Enzyme-induced carbonate precipitation technique for reinforcing underwater sand bed: A feasibility study based on model tests

Qi-Wu Jiang, Ming Huang, Jim S. Shiau, Ling Yang, Ming-Juan Cui, Gui-Xiao Jin, Bin-Cai Huang, Xiao-Ping Zhang

PII: S1674-7755(25)00201-X

DOI: https://doi.org/10.1016/j.jrmge.2025.03.035

Reference: JRMGE 2044

To appear in: Journal of Rock Mechanics and Geotechnical Engineering

Received Date: 12 October 2024
Revised Date: 19 February 2025
Accepted Date: 31 March 2025

Please cite this article as: Jiang Q-W, Huang M, Shiau JS, Yang L, Cui M-J, Jin G-X, Huang B-C, Zhang X-P, Enzyme-induced carbonate precipitation technique for reinforcing underwater sand bed: A feasibility study based on model tests, *Journal of Rock Mechanics and Geotechnical Engineering*, https://doi.org/10.1016/j.jrmge.2025.03.035.

This is a PDF file of an article that has undergone enhancements after acceptance, such as the addition of a cover page and metadata, and formatting for readability, but it is not yet the definitive version of record. This version will undergo additional copyediting, typesetting and review before it is published in its final form, but we are providing this version to give early visibility of the article. Please note that, during the production process, errors may be discovered which could affect the content, and all legal disclaimers that apply to the journal pertain.

© 2025 Institute of Rock and Soil Mechanics, Chinese Academy of Sciences. Published by Elsevier B.V.



Full Length Article

Enzyme-induced carbonate precipitation technique for reinforcing underwater sand bed: A feasibility study based on model tests

Qi-Wu Jiang^{a,b}, Ming Huang^{a,b,*}, Jim S. Shiau^c, Ling Yang^a, Ming-Juan Cui^a, Gui-Xiao Jin^d, Bin-Cai Huang^{a,e} , Xiao-Ping Zhang^b

- a College of Civil Engineering, Fuzhou University, Fuzhou 350108, China
- ^b College of Civil Engineering, Wuhan University, Wuhan 430072, China
- c School of Engineering, University of Southern Queensland, Toowoomba, QLD, 4350, Australia
- d College of Ecological Environment and Urban Construction, Fujian University of Technology, Fuzhou 350118, China
- e Fujian Provincial Investigation, Design & Research Institute of Water Conservancy & Hydropower Co. Ltd., Fuzhou 350118, China

Abstract: Enzyme-Induced Carbonate Precipitation (EICP) is an innovative technique to improve soil strength and reduce permeability. However, the use of EICP for reinforcing underwater sand beds remains largely unexplored. To advance EICP implementation in various geotechnical applications, this paper develops a model box system to investigate the effectiveness of the EICP technique in reinforcing underwater sand beds. An "injection-extraction" system is designed to facilitate the flow of the EICP solution through underwater sand layers. Key parameters, including conductivity, pH, and Ca²⁺ concentration of the solution, are measured and analyzed. Electrical resistivity tomography (ERT) is utilized to evaluate the reinforcement effect in the underwater sand bed. The permeability of the model is tested to verify the feasibility of EICP technology for strengthening underwater sands. Furthermore, scanning electron microscope (SEM) is performed to investigate the growth mechanisms of calcium carbonate (CaCO₃) crystals. The results show that the permeability of the model decreases from 1.28×10-2m/s to 9.66×10-5 m/s, representing a reduction of approximately three orders of magnitude. This verifies that the EICP technology can greatly reduce the permeability of underwater sand beds. With increasing grouting cycles, the resistivity of the underwater sand initially decreases and then increases. This variation in sand resistivity influenced by the ion concentration in the solution, resulting in marked differences in resistivity at various depths and positions within the sand. The findings from this study offer a theoretical basis for the application of EICP technology in reinforcing seabed foundations and supporting marine infrastructure such as offshore pipelines, wind turbines, and oil platforms.

Keywords: Enzyme-induced carbonate precipitation (EICP); Underwater sand reinforcement; Calcium carbonate precipitation; Electrical resistivity tomography (ERT); Sand resistivity; Micromechanism

^{*} Corresponding author. E-mail address: huangming05@fzu.edu.cn

1. Introduction

Engineering projects in challenging geological conditions are often unavoidable. When constructing in areas with highly permeable layers, liquefiable soils, or other adverse geological conditions, it is typically necessary to implement anti-seepage reinforcement measures. These measures help mitigate the impact of groundwater seepage on the stability, safety, and longevity of the structures (e.g. Hafidz et al., 2024; Wang et al., 2024a). The primary goal of these measures is to reduce soil permeability using physical or chemical methods. Conventional soil anti-seepage reinforcement methods, such as pressure grouting, filling, sealing, and surface treatment, can reduce soil permeability to a certain extent. However, these methods are often limited by poor bonding properties, low durability, high costs, and adverse environmental effects (Yang et al., 2016). In the context of the current global push for green and sustainable development, these limitations are becoming increasingly problematic (Sun et al., 2024a). As a result, there is a pressing need to develop innovative and environmentally friendly soil anti-seepage reinforcement technologies.

Enzyme-induced carbonate precipitation (EICP) is an emerging biotechnological technique for soil stabilization, showing great potential in various geotechnical applications (e.g. Arab et al., 2021; Li et al., 2022; Liu et al., 2023; Wang et al., 2023a). This technique offers a broad range of material sources and is relatively easy to implement, making it more environmentally friendly by reducing carbon emissions and energy consumption (e.g. Park et al., 2014; Nam et al., 2015; Zhang et al., 2023a). Numerous studies have demonstrated its adaptability for reinforcing various soil types, including Ottawa 20-30 sand, desert sands, and other granular soils (e.g. Gao et al., 2019a; Cui et al., 2021; Montoya et al., 2021; Wu et al., 2024). By utilizing free urease extracted from plants, the EICP technique lowers construction costs in various geotechnical applications (e.g. Khodadadi et al., 2020; Xu et al., 2023a), such as soil improvement (e.g. Wang et al., 2023b; Jiang et al., 2024a), dust control (e.g. Song et al., 2020, Sun et al., 2021), heavy metal immobilization (e.g. Xue et al., 2022; Huang et al., 2024a) and thermal conductivity improvement (e.g. Li et al., 2023a, b). Many studies have reported improvements in soil properties using the EICP technique, including enhanced micro-mechanical properties (e.g. Huang et al., 2021; Liu et al., 2024), macro-mechanical properties (e.g. Xiao et al., 2018; Montoy et al., 2021), liquefaction resistance (Xiao et al., 2020), and corrosion inhibition (e.g. Sun et al., 2023; Wang et al., 2024b). Additionally, the EICP solution exhibits superior fluidity and diffusivity, allowing it to penetrate fine soil pores more effectively than conventional methods. This characteristic enhances its applicability in practical engineering situations (e.g. Jiang et al., 2016; Meng et al., 2021; Huang et al., 2024b). In summary, EICP technology provides significant advantages in both seepage prevention and soil reinforcement, presenting promising prospects for various engineering applications

Several researchers have conducted extensive research on the impermeability of bio-cemented soil under unsaturated conditions (e.g. Martinez et al., 2014; Gomez et al., 2017). Chu et al. (2013) applied bio-cementation technology in the construction of a water reservoir. The results showed that the permeability of the sandy soil decreased from 10^{-4} m/s to 10^{-7} m/s, a significant reduction of approximately three orders of magnitude in hydraulic conductivity. Gao et al. (2019a) incorporated bio-cementation technology into seepage control for canals, utilizing four different reinforcement methods for stabilizing canal surfaces. The results indicated that the leakage rate of samples treated with these four methods could be reduced by 1/379 of the original. Nafisi et al. (2019) reported that the hydraulic conductivity of three types of sands with varying particle sizes decreased by more than one order of magnitude following EICP treatment. Jiang et al. (2024b) also observed a substantial reduction in hydraulic conductivity after EICP treatment, with the permeability of the specimen decreasing by more than two orders of magnitude. Numerous studies have demonstrated that the hydraulic conductivity of soils treated with EICP technique is reduced by two orders of magnitude or more (Cheng et al., 2017; Do et al., 2019; Zamani et al., 2019). However, the studies mentioned above concerning the effectiveness of EICP technology were primarily conducted under unsaturated conditions. The application of EICP technique for reinforcing sandy soil in saturated water environments is considerably under-researched. To advance EICP implementation in various geotechnical applications, more efforts should be made to investigate the effectiveness of the EICP technique in reinforcing underwater sand beds prior to field applications.

Furthermore, it is essential to utilize effective and nondestructive monitoring methods for evaluating the reinforcement effect of saturated soil. Electrical resistivity tomography (ERT) is one of the most widely used geophysical techniques (e.g. Loke et al., 2013; Tucker et al., 2015). It enables the identification of subsurface resistivity distributions based on surface measurements and has been successfully applied in various fields, including geological surveys, structural health monitoring, agricultural studies, and contaminant detection (Bearce et al., 2016). During the EICP mineralization process, ERT can capture resistivity changes caused by spatial variations in the soil matrix and solution concentration, thereby effectively assessing the reinforcement effect. Zhang et al. (2024) employed three-dimensional (3D) ERT to monitor the biocementation process of a sand-packed column and collected electrical responses at various treatment stages along with the calcium carbonate (CaCO₃) contents. Shi et al. (2024) conducted electrical resistivity measurement techniques to investigate the electricity resistivity of MICP-treated calcareous sand foundation based on model tests. Consequently, ERT has been proven to be an effective tool for assessing the reinforcement effect of sand treated with EICP technology.

This study investigates the reinforcement effect of an underwater sand bed using EICP technique based on model tests. Conductivity, pH, and Ca²⁺ concentration measurements were taken from embedded and extraction pipes to assess the extent of EICP mineralization reactions. ERT was employed to monitor the reinforcement effect of the underwater sand bed. The overall permeability of the model was evaluated to validate the feasibility of EICP technology for reinforcing underwater sandy soils. The results in this study establish a theoretical basis for the application of the EICP technique in the reinforcement of seabed foundation and the mitigation of submarine landslides.

2. Model tests and materials

2.1. Model box system and "injection-extraction" system

2.1.1. Model box system

Fig. 1 shows the model box system that is designed to simulate the reinforcement of underwater soil using EICP technique. The model box system includes the following components: model box, perforated steel plates, geotextile, inner and outer grouting pipes, suction pipe, grouting and pumping equipment, and ERT measurement lines. As illustrated in Figs. 1 and 2, the model box enclosure is constructed by welding and assembling 2 mm thick steel plates, resulting in dimensions of 2 m in length, 1.6 m in width, and 1 m in height. The overall shape of the enclosure is a rectangular prism without a lid. The model box is divided into three segments along its length in a ratio of 1:8:1. The central segment measures $1.6 \text{ m} \times 1.6 \text{ m} \times 1 \text{ m}$, while the water storage segments at both ends measure $0.2 \text{ m} \times 1.6 \text{ m} \times 1 \text{ m}$. The central segment of the model box is filled with field sand, while the water storage segments are filled with water. Two perforated steel plates separate the central segment from the water storage segments at both ends. These perforated plates primarily simulate a saturated water environment, allowing water to flow freely from the storage segments into the central segment of the model box. To prevent sand from entering the water storage segments, geotextiles are placed on both perforated steel plates, acting as sand-retaining barriers. Four grouting pipes are arranged around the sand, positioned 20 cm from the model box. Additionally, a suction pipe is located at the center of the sand, 80 cm from the model box. Three ERT survey lines are arranged on the sand surface, with each line featuring 60 high-density resistivity electrodes. These ERT lines can measure the resistivity of the sand at diverse depths within the same cross-section. The water head difference can be controlled through the inlets and outlets to assess the permeability of the model before and after reinforcement.

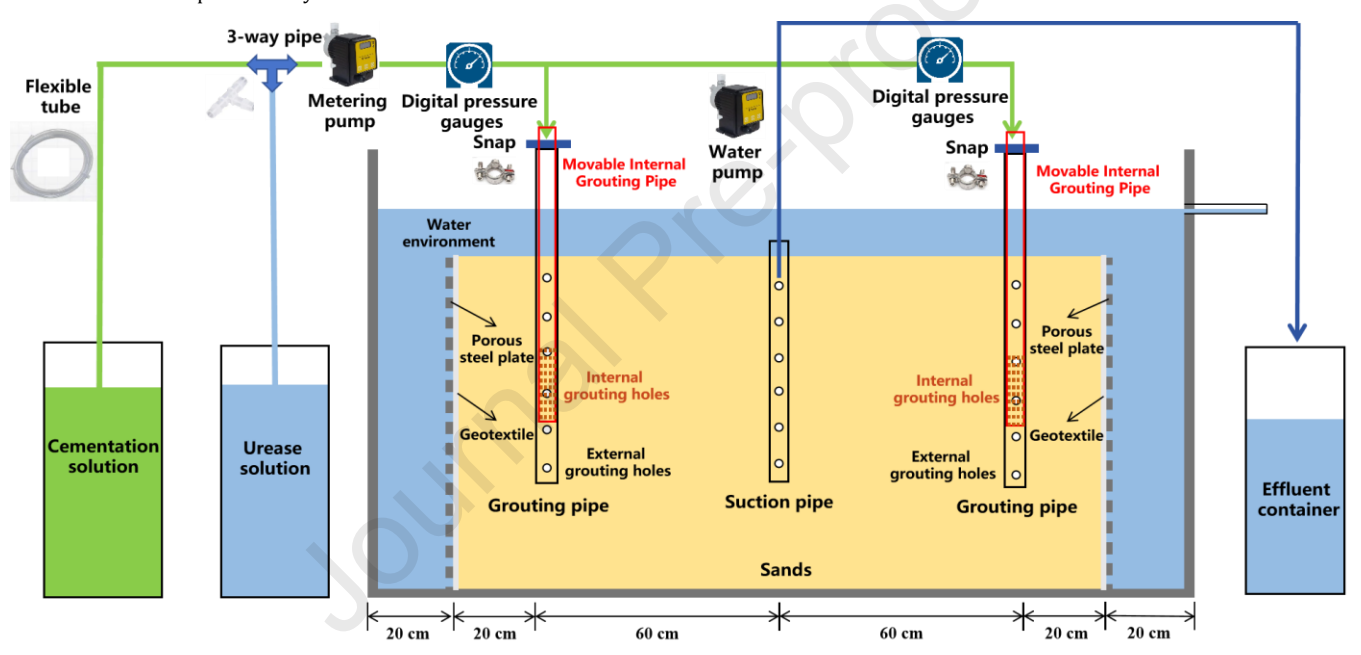


Fig. 1. Schematic diagram of the model box system design.

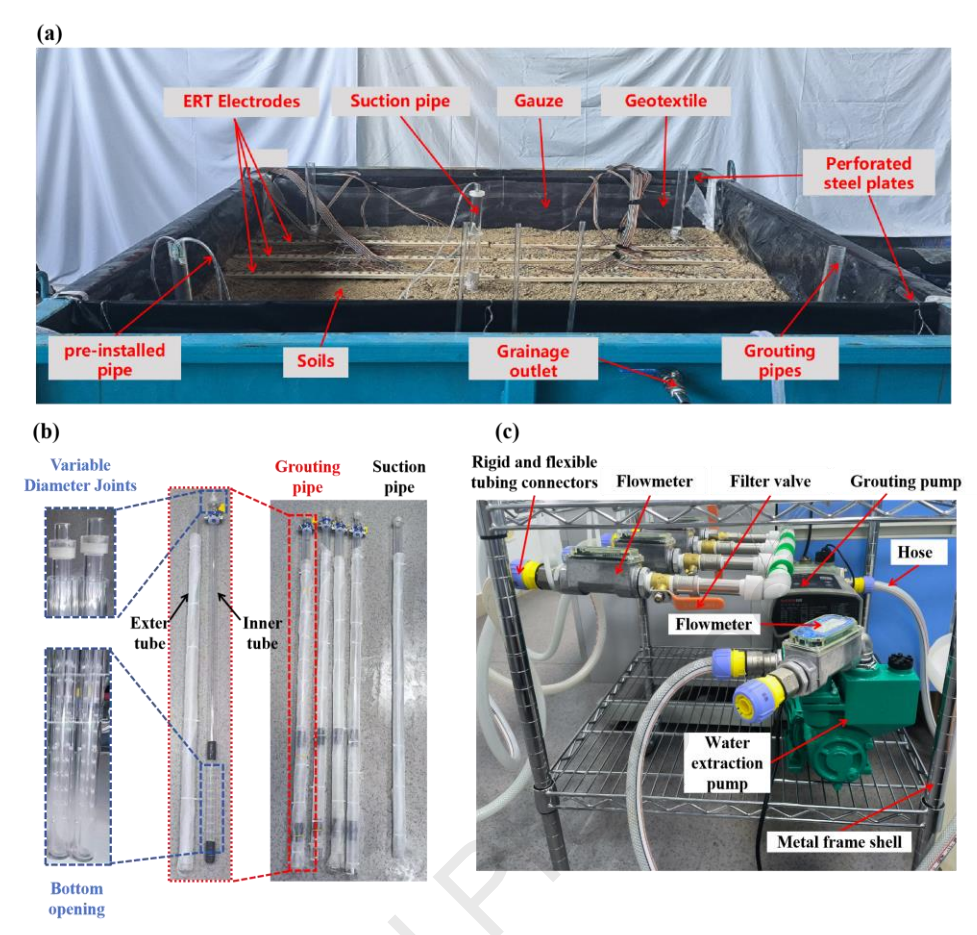


Fig. 2. Overview of model box system: (a) model box system; (b) suction pipes and grouting pipes; and (c) Grouting equipment and pumping equipment.

2.1.2. "Injection-extraction" system

The pumping and grouting equipment primarily consists of a metal frame shell, grouting pump, water extraction pump, filter valve, flowmeter, pressure gage, flexible tubing, tubing connectors, and valve switches (see Fig. 2c). The metal frame shell protects the grouting pump, water extraction pump, and associated water pipes. The grouting pump and water extraction pump provide the necessary power for extracting and pumping slurries. The filter valve, located at the front of the water pipes, is responsible for filtering out debris that may inadvertently enter the processing fluid. The flowmeter controls the volume of the solution extracted and grouted, allowing for subsequent measurements of the solution's pH, conductivity, and calcium ion concentration at different extracted volumes. These indicators indirectly reflect the cementation effectiveness within the model box. The pressure gage monitors the grouting pressure, as both excessive and insufficient pressure can adversely affect the test results. In the model test, four grouting pipes require tee pipes to split the water flow into four streams, enabling simultaneous grouting. Four PVC rigid-to-flexible tubing adapters are used to connect the tee pipes.

Several researchers have observed that the application of the EICP technique to large-scale sand often results in significant unevenness in reinforcement effects (e.g. Zeng et al., 2021, 2022; Xu et al., 2023b). To address this challenge and achieve gradual consolidation of large-scale sands, inner and outer grouting pipes have been designed for step-by-step reinforcement of the sand at varying depths (Fig. 2b). Initially, the inner pipe is positioned at the bottom of the model, and as reinforcement progresses, it is gradually moved upwards. As the inner pipe ascends, the reinforced zone shifts upward as well, facilitating the gradual consolidation of the large-scale sandy soil. During the reinforcement process, the outer grouting pipe remains stationary within the sand, while the slightly smaller inner grouting pipe is allowed to move freely. The arrangement of the inner and outer grouting pipes helps reduce the vertical unevenness associated with the EICP technique. To further minimize horizontal unevenness, the extraction pipe is centrally positioned within the model. During the injection of the cementation solution and urease solution, water is concurrently extracted from the model via the suction pipe, thereby enhancing the horizontal diffusion radius of the EICP solution.

2.2. Materials

2.2.1. Tested Sands

The sand used in the experiment was collected from a typical sand layer near Guanxun Stream in Xiamen City, Fujian Province, China. The chloride ion content complies with the requirements set by Chinese standards (JGJ 52-2006, 2006; GB/T 14684-2011, 2011). The particle size distribution curve of the sand is shown in Fig. 3b, revealing that the particle diameters range from 0.1 to 4 mm. Specifically, D_{60} is 1.6 mm, D_{30} is 0.7 mm, D_{10} is 0.35 mm, and the average particle diameter (D_{50}) is 1.35 mm. The sand exhibits poor grading, characterized by an unevenness coefficient (C_{0}) of 4.57 and a curvature coefficient (C_{0}) of 0.875. The void ratio of the sea sand is 0.53, and its density is 1.47 g/cm³.

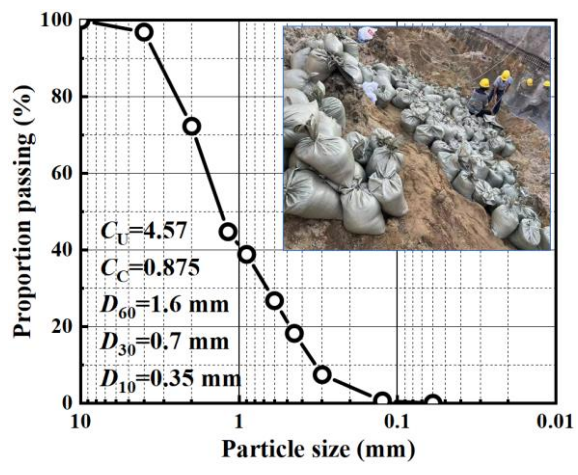


Fig. 3. Grain size distribution curve of Sands used in this model tests

2.2.2. Cementation solution

The cementation solution used in this study consists of calcium chloride and urea. Specifically, in the EICP mineralization reaction, calcium chloride primarily provides calcium ions, while urea serves as a substrate for urease hydrolysis, supplying carbonate ions. These ions subsequently combine to form CaCO₃ precipitates. Previous studies have demonstrated that the insufficient solution concentration may yield inadequate CaCO₃ precipitation for effective particle cementation, while excessive calcium ion concentrations could suppress urease activity and thereby hinder carbonate formation (Xu et al., 2023c). After careful consideration, the cementation solution concentration of 1.5 mol/L was selected for this study, with a volume ratio of soybean urease to cementation solution set at 1:1. Fig. 4d illustrates the preparation process of the cementation solution.

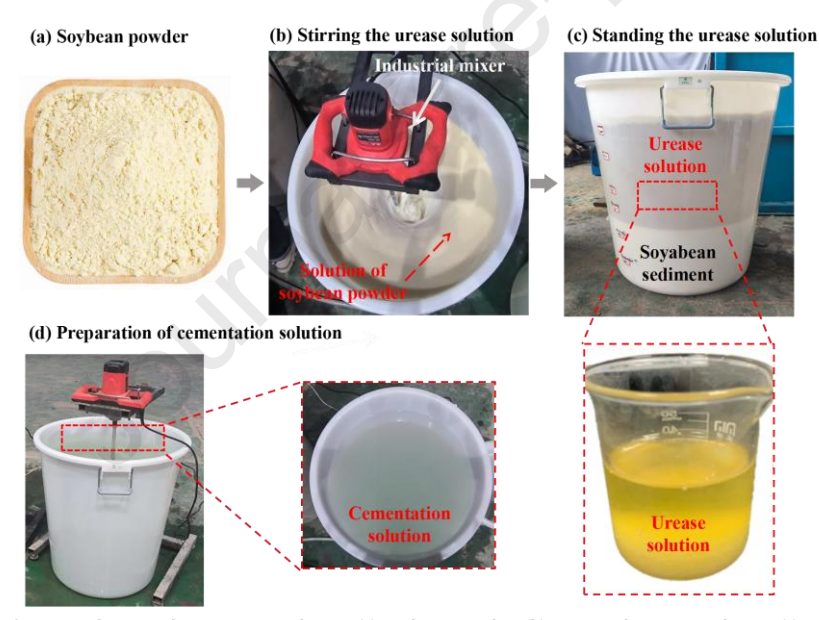


Fig. 4. Preparation process of urease solution and cementation solution: (a) Soybean powder; (b) Stirring the urease solution; (c) Standing the urease solution; and (d) Preparation of cementation solution.

2.2.3. Soybean urease solution

The soybean urease solution was prepared using a modified plant-derived enzyme extraction method (Cui et al., 2024). The soybeans used in this study were sourced from Heze, Shandong Province, China. Fig. 4 illustrates the preparation process of the urease solution, which involves the following three steps: (1) The soybeans were thoroughly dried in a drying oven, ground into a powder, and then sieved using a No. 100 mesh sieve. The soybean powder was stored in a dry environment at 4 °C for future experimental use; (2) Every 100 g of soybean powder was mixed with 1 L of water containing 0.01 mol/L CaCl₂, and the mixture was stirred at 500 rpm for 20 min. The addition of 0.01 mol/L CaCl₂ aimed to reduce the turbidity of the solution (Lai et al., 2024); and (3) Gravitational stratification occurred during 12-h quiescent settling, yielding a lower phase of soybean residue (discarded) and an upper crude urease solution (utilized for subsequent experiments).

2.3. Model preparation and injection scheme

2.3.1. Model preparation

The model preparation involved several steps:

- (1) A geotextile layer was installed inside the model box. Holes were punched on both sides of the geotextile, corresponding precisely in position and size to those in the perforated steel plates.
- (2) A layer of gauze was laid over the geotextile to prevent sand particles from escaping through the holes. This allowed water to freely permeate, thereby establishing a saturated water environment.
- (3) Four grouting pipes were positioned at the four corners of the model box, 20 cm from each side. A suction pipe was placed at the center, 60 cm from both steel plates. Simultaneous grouting and suction were employed to enhance the diffusion radius of the EICP solution and mitigate the inherent heterogeneity of the EICP technique.
- (4) A layered backfill method was employed, with each layer of sand being 10 cm thick. Upon reaching the designated height, the surface was leveled using a tamping tool. This process was then repeated until the desired backfill height was attained.
- (5) During backfilling, embedded tubes were installed in stages based on the sand height: tube B at 20 cm, tubes A, C, E, and F at 40 cm, and tube D at 60 cm. After grouting was completed, the solution was extracted through these tubes to measure conductivity, pH, and calcium ion concentration, indirectly reflecting the internal cementation status.
- (6) Three ERT lines were fixed on the sand surface in consistent positions: line 1 near the suction pipe, line 2 between the suction pipe and grouting pipe, and line 3 near the grouting pipe. Electrical resistivity measurements were taken at these three locations. Resistivity served as an indirect indicator of ion migration and diffusion, thus reflecting the cementation level of the internal sand.

2.3.2. Grouting scheme

A single-phase grouting method was employed, utilizing 100 L of crude urease solution and 100 L of cementing solution per batch. These solutions were mixed within a three-way valve and then injected into the model box through grouting equipment. The grouting pressure was set at 0.2 MPa to ensure effective injection. This value was chosen to minimize the risk of damaging previously formed CaCO₃, during subsequent grouting cycles. Grouting was conducted simultaneously through four injection tubes, with flow meters ensuring uniform delivery of the EICP solution. To enhance the diffusion radius of the EICP solution and improve sand cementation within the model, the grouting and extraction equipment were operated simultaneously. At extraction volumes of 50 L, 100 L, 150 L, and 200 L (representing 25%, 50%, 75%, and 100% of the total volume), the extracted fluid was collected for analysis of parameters, e.g. calcium ion concentration, electrical conductivity, pH. After grouting, fluids from six embedded tubes (A-F) were also sampled for the same analyses. This sequence constituted one grouting cycle, with an interval of 2 d between cycles to allow sufficient reaction of the EICP solution within the model. The grouting process was repeated 10 times, with the internal injection tubes raised by 10 cm after every two cycles to achieve gradual depth-wise reinforcement.

2.4. Test methods

2.4.1. Electrical resistivity test

The ERT method, a geophysical exploration technique, is based on the fundamental principle of utilizing resistivity differences (e.g. Zhang et al., 2023b, 2024). For this experiment, the Wenner array (α) configuration was employed as the primary measurement method, with the electrode arrangement and traverse layout illustrated in Fig. 5a. Initially, the electrode groups AM, MN, and NB were employed from left to right at a fixed unit electrode spacing, acquiring data points corresponding to the first subsurface layer. As the experiment progressed, the electrode spacing was gradually increased. This enabled the AM, MN, and NB groups to collect data at double the unit spacing, thereby acquiring data for the second subsurface layer. This process continued with increases in electrode spacing, enabling the collection of data points at varying depths below the surface, ultimately producing a trapezoidal resistivity profile.

Because the ERT method is commonly used for field detection with electrode spacings typically ranging from 1 m to 5 m, it is unsuitable for direct application in the model tests. To solve this problem, the ERT measurement lines were specifically designed for the model test, as illustrated in Fig. 5c. The preparation materials for the ERT measurement lines primarily consisted of aviation connector, ribbon cable, copper screws, and wooden boards for electrode fixation. The preparation process of ERT measurement lines primarily includes wires to plugs welding, wires to screws welding, and welds encapsulatin. The layout of the ERT measurement lines is shown in Fig. 5b. It consisted of three lines positioned on the sand surface. Each line is composed of 60 high-density resistivity electrodes. Each measurement recorded the apparent resistivity values of the sand at different depths within the same cross-section.

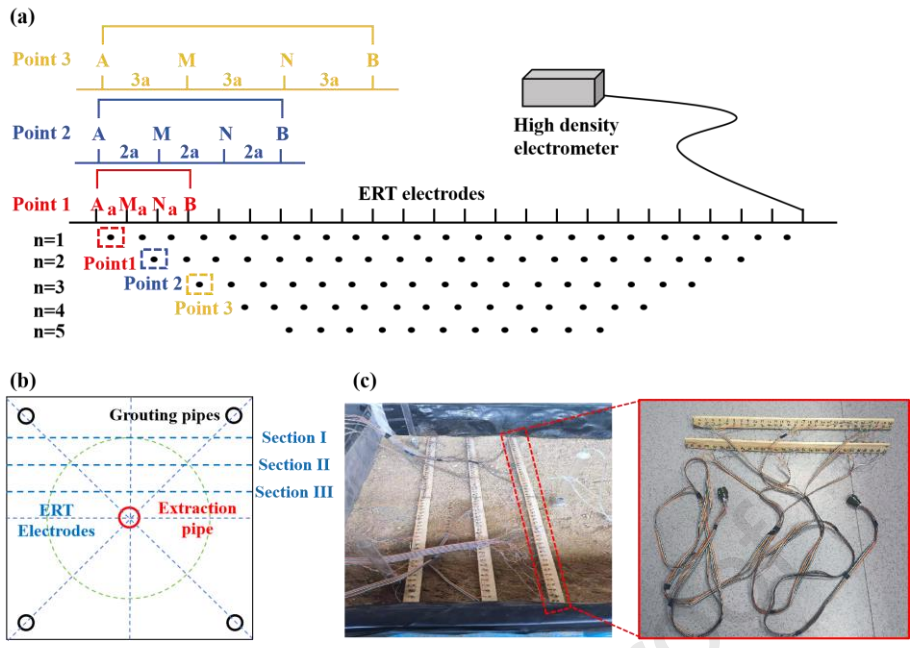


Fig. 5. Basic principles of ERT and location of ERT Line: (a) basic principles of ERT; (b) location of ERT measurement lines; and (c) ERT measurement lines.

2.4.2. Permeability test

The permeability of the model was measured following the initial (0th) and the subsequent 2nd, 4th, 6th, 8th, and 10th grouting cycle. Water was injected through the inlet on the right side, while the drain outlet on the left side was opened to create a significant head difference. This head difference was maintained for a specific duration to establish a stable seepage flow. The volume of seepage collected at the left drain outlet was recorded over 5 min, with each test repeated three times. The average value was then used as the final result. The permeability measurement process for the model is shown in Fig. 6, and the coefficient of permeability k was calculated as

$$k = \frac{QL}{At\Delta h} \tag{1}$$

where k is the permeability of the model, Q is the seepage volume, L is the width of the model, A is the cross-sectional area of the model, Δh is the water level difference, and t is the seepage time.

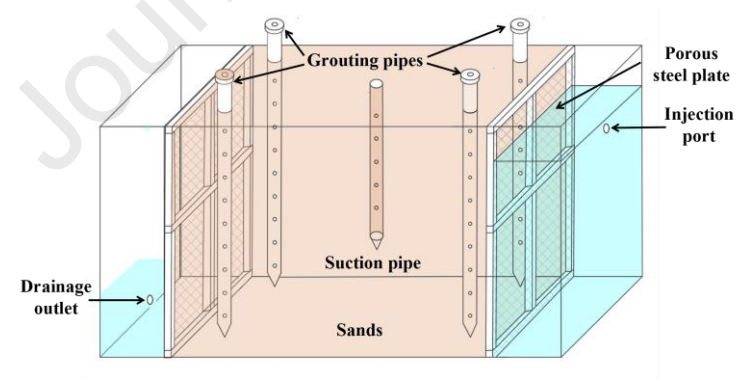


Fig. 6. Schematic diagram of model permeability test.

2.4.3. Conductivity, pH and Ca^{2+} concentration of the solution

Conductivity and pH serve as indirect indicators of the diffusion extent of the solution and the reinforcement effectiveness in the sand (Zeng et al., 2021). Meanwhile, the calcium ion concentration provides an indirect measure of the urease-catalyzed decomposition of urea. In Fig.7, six detection tubes (A-F) were embedded into the model at specific locations. Tubes A, C, E, and F were placed at a depth of 40 cm, while tubes B and D were embedded at 20 cm and 60 cm, respectively. After each grouting cycle, a peristaltic pump was used to extract small volumes (less than 20 ml) of the solution. The extracted solution was immediately collected for of conductivity, pH, and Ca²⁺ concentration measurement, with detailed records maintained. When the extracted grout volume reached 25%, 50%, 75%, and 100% of the total injected grout volume, 100 mL of solution was collected using a beaker to measure conductivity, pH, and Ca²⁺ concentration from the extraction tubes. The Ca²⁺ concentration was determined using the ethylene diamine tetraacetic acid (EDTA) method (e.g. Choi et al., 2017; Lai et al., 2021), while conductivity and pH were measured using a conductivity meter and a pH meter, respectively.

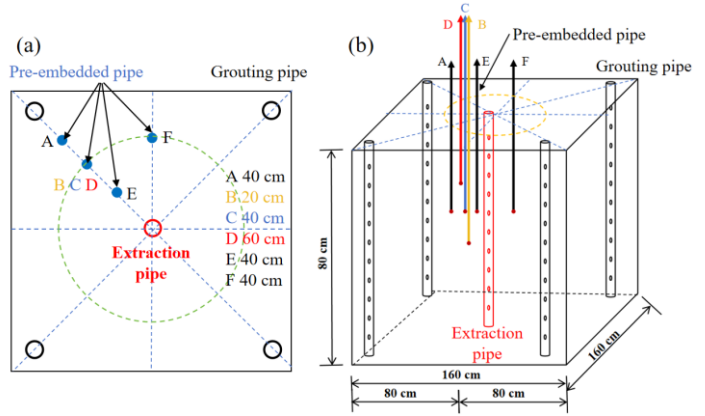


Fig. 7. Schematic diagram of pre-embedded pipe location: (a) horizontal position; and (b) elevation position.

2.4.4. SEM

In this study, the SEM analysis was performed using an FEI CZECH REPUBLIC S.R.O., field-emission scanning electron microscope (FE-SEM) operated at a specimen acceleration voltage of 15 kV. After gold coating treatment, SEM was performed to analyze the internal characteristics and structure of the EICP-treated specimens. The SEM images reveal the distribution and morphology of CaCO₃ precipitates formed via EICP and are useful in identifying the extent of mineralization, crystal size, and attachment between sand particles.

3. Results of model tests

3.1. Conductivity, pH and Ca²⁺ concentration of the solution from the extraction pipe

The values of conductivity, pH, and Ca²⁺ concentration in the solution extracted through the extraction pipe can serve as indirect indicators of the extent of EICP mineralization reactions. A flowmeter was installed on the extraction pipe to monitor these parameters. The Ca²⁺ concentration, conductivity, and pH were measured when the extracted solution volume reached 25%, 50%, 75%, and 100% of the total grouting volume. Fig. 8a shows the conductivity results of the solution extracted through the extraction pipe during different grouting cycles. As illustrated, the solution's conductivity increases progressively with each grouting cycle. After the first grouting cycle, the conductivity is approximately 10 ms/cm, increasing to 150 ms/cm after the 10th cycle, indicating a 15-fold increase. This sharp rise is primarily due to the decomposition of urea by urease, which produces CaCO₃ and NH₄+, thereby increasing the ionic content in the solution. Since conductivity correlates with ionic concentration, the continuous decomposition of urea leads to higher ion concentrations, resulting in an increase in conductivity. Moreover, analyzing the conductivity after the second grouting cycle reveals that at 25%, 50%, 75%, and 100% extraction volumes, the conductivity of the solution is 27.7 ms/cm, 29.1 ms/cm, 32.8 ms/cm, and 33.8 ms/cm, respectively (Fig. 8a). A slight increase in solution conductivity is observed with an increasing extraction volume. Notably, at 25% extraction, the solution near the extraction pipe is primarily withdrawn, while at 100% extraction, the solution farther away is sampled. This suggests that mineralization reactions are more intense in areas farther from the extraction pipe, resulting in higher ionic concentrations in those regions.

Fig. 8b illustrates the pH of the solution extracted through the extraction pipe over different grouting cycles. As shown, the pH gradually decreases with each successive cycle. This decline is mainly due to Ca^{2+} combining with CO_3^{2-} to form $CaCO_3$, this process depletes CO_3^{2-} and promotes the ionization of HCO_3^{-} . The increased H^+ concentration in the solution ultimately lowers the pH (Weng et al., 2024). The pH of the solution ranges from 6.8 to 7.6, indicating a near-neutral environment, which is consistent with the pH variation observed during $CaCO_3$ precipitation in the EICP mineralization process.

Fig. 8c shows the Ca^{2+} concentration of the solution extracted through the extraction pipe across different grouting cycles. Fig. 8 indicates that between 1 to 5 grouting cycles, the Ca^{2+} concentration ranges from 0.01 mol/L to 0.06 mol/L, while between 6 to 10 grouting cycles, it increases slightly, ranging from 0.02 mol/L to 0.07 mol/L. Notably, the Ca^{2+} concentration in the solution maintains a consistently low level, remaining below 0.1 mol/L (Fig. 8c). Two primary factors contribute to this: first, a substantial portion of the injected Ca^{2+} combines with CO_3^{2-} produced by urea decomposition to form $CaCO_3$, leaving only a small fraction of free Ca^{2+} in the solution. Second, the model test is conducted in a saturated water environment, where the injected cementing solution is diluted by the surrounding water, keeping the Ca^{2+} concentrations consistently below 0.1 mol/L. Additionally, Fig. 8 shows that as the volume of extracted solution increases, the Ca^{2+} concentration gradually rises. This increase may result from the extraction of larger volumes of solution from regions adjacent to the grouting pipe, where the Ca^{2+} concentration is higher.

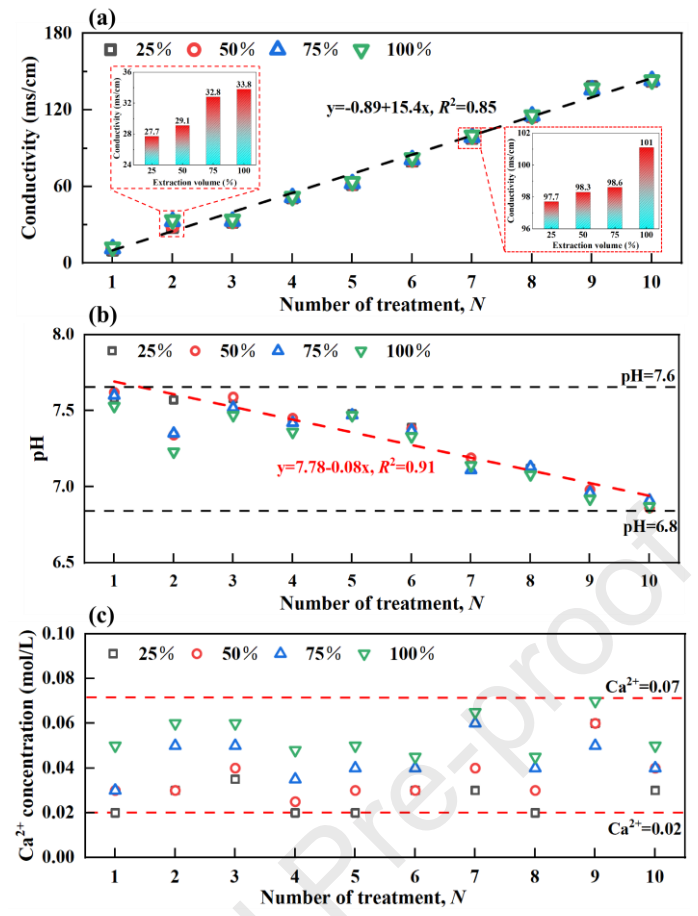


Fig. 8. Grouting pipe test results under different grouting numbers: (a) conductivity; (b) pH; and (c) Ca2+ concentration.

3.2. Conductivity, pH and Ca^{2+} concentration of the solution from the pre-embedded pipe

Fig. 9a presents the conductivity results of pre-embedded pipes under different grouting cycles. As shown in Fig. 9a, the conductivity of all six pipes (A-F) progressively increases with each grouting cycle. For example, the conductivity of Pipe F is only 10.6 ms/cm after the first cycle, but it rises to 156.7 ms/cm by the 10th cycle, representing nearly a 15-fold increase. This significant rise is primarily due to the accumulation of ion concentration in the solution as the grouting cycles progress, which in turn raises the conductivity. Furthermore, Fig. 9a shows that under the same grouting cycle, the conductivity of the solutions at locations A and B exceeds that at other locations. For example, after the second grouting cycle, the conductivities of pipes A and B were 51.1 ms/cm and 46.8 ms/cm, respectively, while those of pipes C, D, E, and F were 26.1 ms/cm, 25.1 ms/cm, 23.6 ms/cm, and 21.1 ms/cm, respectively. This difference is primarily attributable to the closer proximity of pipes A and B to the grouting pipe, where the majority of the injected cementitious and urease solutions accumulate, resulting in higher conductivity at these locations during the grouting cycles. Additionally, the conductivity of the solution at location F remains consistently lower than at other locations. This is primarily because Pipe F is situated farther from both the grouting and suction pipes and is not along the seepage path between them. As a result, there is less accumulation of EICP solution at location F, leading to weaker EICP mineralization reactions and, consequently, lower conductivity.

Fig. 9b presents the pH results of pre-embedded pipes under different grouting cycles. Fig. 9b shows that as the number of grouting cycles increases, the pH values of the solution in six pipes generally trend downward. This decrease is primarily due to the reaction between Ca^{2+} and CO_3^{2-} in the solution, resulting in the formation of $CaCO_3$. The consumption of CO_3^{2-} facilitates the ionization of HCO_3^{-} , leading to a sharp increase in H^+ , which subsequently lowers the pH of the solution. The extent of the pH decrease can also indirectly indicate the degree of the EICP mineralization reaction.

Fig. 9c presents the Ca^{2+} concentration results of pre-embedded pipes under varying grouting cycles. During the initial stage of grouting reinforcement, the Ca^{2+} concentrations at pipes A and B were higher, while those at pipes C and D were lower. For example, in the first grouting cycle, the Ca^{2+} concentrations at locations A and B were 0.25 mol/L and 0.20 mol/L, respectively, whereas those at locations C and D were 0.08 mol/L and 0.07 mol/L, respectively. This difference was primarily due to the positioning of the internal injection pipe at the bottom during the initial grouting stage, resulting in the majority of the injected EICP solution accumulating in the lower area of the model.

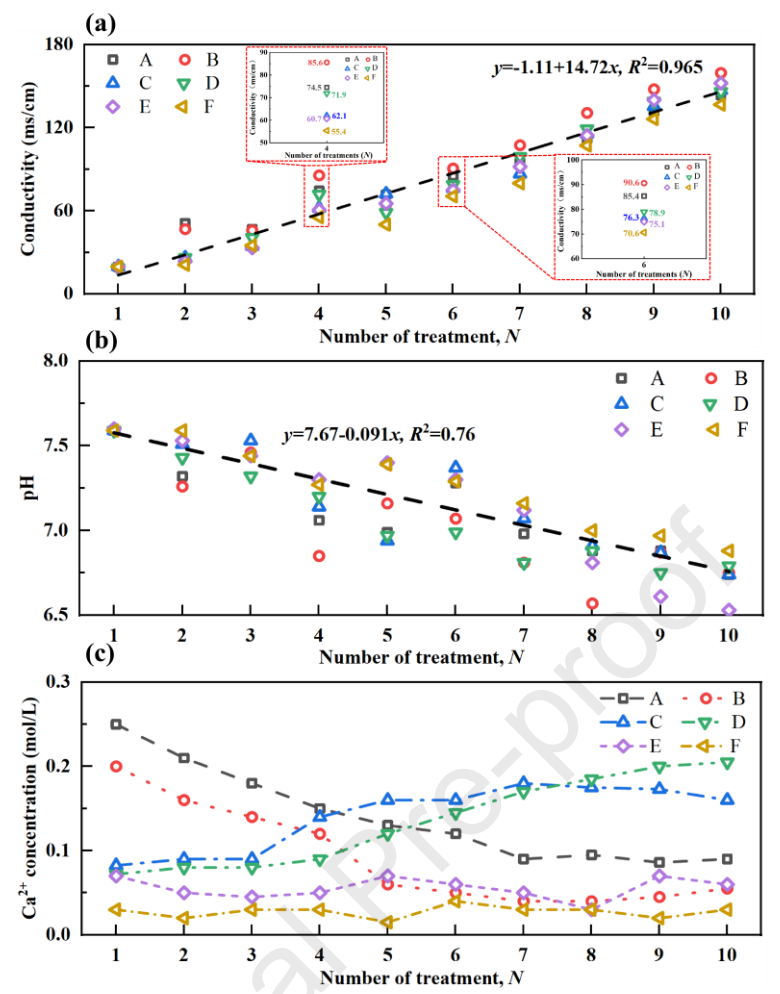


Fig. 9. Pre-embedded pipe test results under different grouting numbers: (a) conductivity; (b) pH; and (c) Ca2+ concentration.

Furthermore, as the number of grouting cycles increased, the Ca²⁺ concentrations at locations A and B gradually decreased, while those at locations C and D gradually increased. This trend could be attributed to the upward movement of the internal injection pipe with each subsequent grouting cycle, which increased the depth of the injected EICP solution. The altered position of the internal injection pipe resulted in changes in the location of the injected solution, thereby causing variations in the Ca²⁺ concentrations at the different pre-embedded pipes. In contrast, the Ca²⁺ concentrations at locations E and F remained relatively constant, hovering around 0.05 mol/L. This consistency was due to the distance of pipes E and F from the injection pipe, which made it difficult for the injected EICP solution to diffuse to these locations.

3.3. Variations of sand resistivity with different grouting cycles

Fig. 10 illustrates the variations in sand resistivity across different grouting cycles. As shown in Fig. 10, the apparent resistivity of the sand transitions gradually from red to yellow and subsequently to blue with progressive grouting cycles. The areas of red and yellow diminish, while those of blue and green expand correspondingly. The different colors signify varying resistivity levels within the respective regions, where red indicates a higher resistivity, and blue/green indicates lower resistivity. This phenomenon reflects a gradual decrease in sand resistivity as the grouting cycles progress. This change is primarily attributed to the significant influence of NH₄* and Ca²* in the solution on sand resistivity (e.g. Zhang et al., 2015; Wang et al., 2017). The injected urease solution decomposes urea to generate Ca²* and NH₄*, while the cementing solution also contains Ca²*, contributing to a gradual increase in ionic composition and concentration within the solution. Consequently, with progressive grouting cycles, the high-resistivity regions of sand decrease, while low-resistivity areas expand.

Fig. 10 illustrates significant differences in the resistivity variation patterns of sands at varying depths and locations, indicating notable unevenness in the EICP reinforcement efficacy of large-scale model tests. Existing studies on the non-uniformity of EICP-treated large-scale samples have primarily focused on aspects such as strength, stiffness, and apparent cementation effects (e.g. Martinez et al., 2014; Gomez et al., 2017). The apparent resistivity of the sand in the central region appears red, indicating relatively high resistivity, whereas the sand on both sides exhibits yellow or blue hues, signifying lower resistivity. This difference is primarily due to the placement of the grouting pipes at the sides, through which the EICP solution flows toward the suction pipes. Consequently, most of the EICP solution is distributed between the grouting and suction pipes, resulting in lower concentrations of EICP solution near the suction pipes. As a result, higher resistivity is observed in the central region of the model.

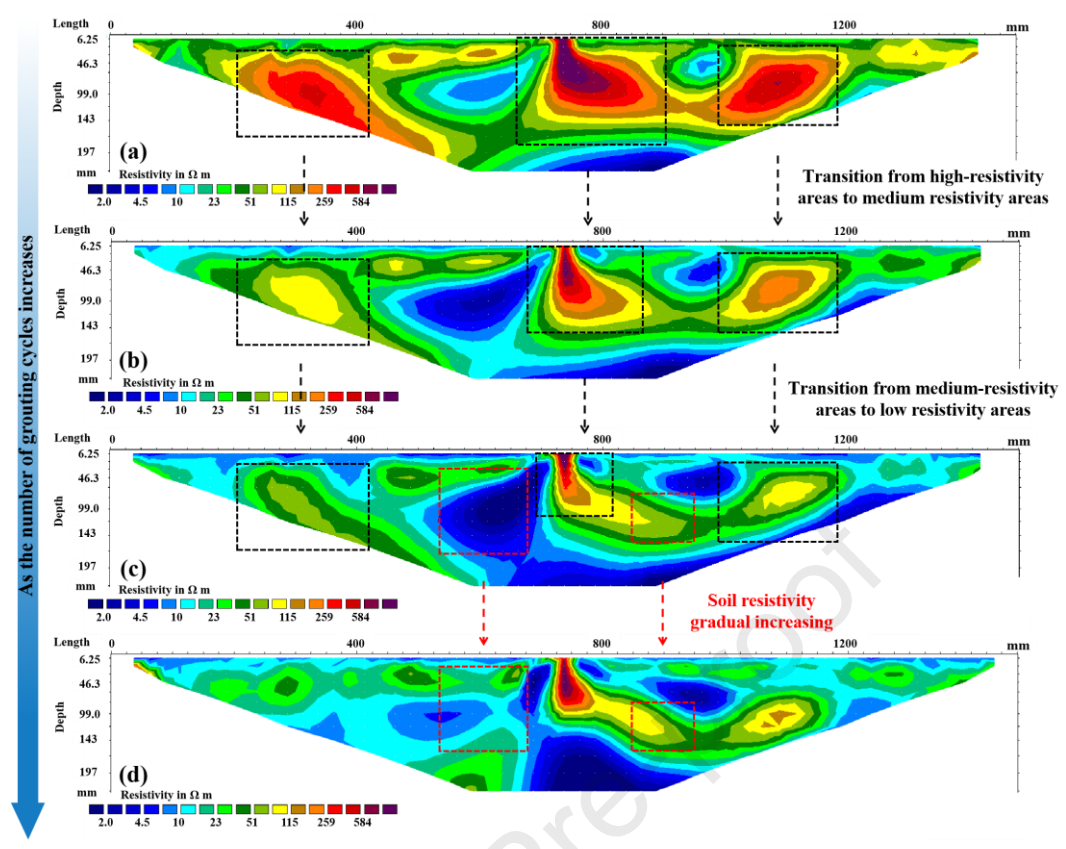


Fig. 10. Variations of sand resistivity under different grouting cycles: (a) 1 cycle; (b) 2 cycles; (c) 3 cycles; and (d) 5 cycles.

To further analyze the variation in sand resistivity, the data points obtained from the ERT method are categorized based on both depth and position. Specifically, the sand resistivity data are divided vertically into four layers, with data points from the fifth, tenth, fifteenth, and twentieth rows designated as the first, second, third, and fourth layers, respectively. Horizontally, the sand resistivity data are divided into six columns, where the 5th, 10th, 15th, 20th, 25th, and 30th data points, counted from the leftmost within each layer, are selected as points A-F, respectively.

Fig. 11 illustrates the variations in sand resistivity with reinforcement cycles at different locations and depths. As shown in Fig. 11, as the number of grouting cycles increases, the sand resistivity at various locations exhibits a consistent trend. During the initial stages of grouting, the resistivity of the sand decreases significantly, dropping from approximately 30 Ω m to around 10 Ω m, corresponding a reduction of 20 Ω m (Fig. 11a). This marked decline is primarily attributed to the increasing ionic concentration in the solution, as previously explained. However, during the later stages of grouting, an inverse trend is observed, with the resistivity values of the sand rising with subsequent grouting cycles. For instance, the resistivity at location A after the fourth grouting cycle is 6.08 Ω m, which increases to 10.94 Ω m following the fifth grouting cycle, indicating an increase of 4.86 Ω m. Similar patterns are observed across different depths and horizontal positions, suggesting that this phenomenon is neither accidental nor a result of experimental error. Comparable behavior has also been reported in the model experiments conducted by Shi et al. (2024). This phenomenon may be attributed to the gradual blocking of pores in the sand due to the precipitation of CaCO₃ crystals. This blocking effect reduces the availability of ion exchange channels, subsequently lowering the ionic concentration and contributing to the rise in resistivity. At this stage, the formation of CaCO₃ in the sand becomes the dominant factor influencing sand resistivity. In Section 4.2, a mechanistic explanation for this intriguing phenomenon is provided, specifically focusing on the influence of CaCO₃ on sand resistivity in a saturated environment.

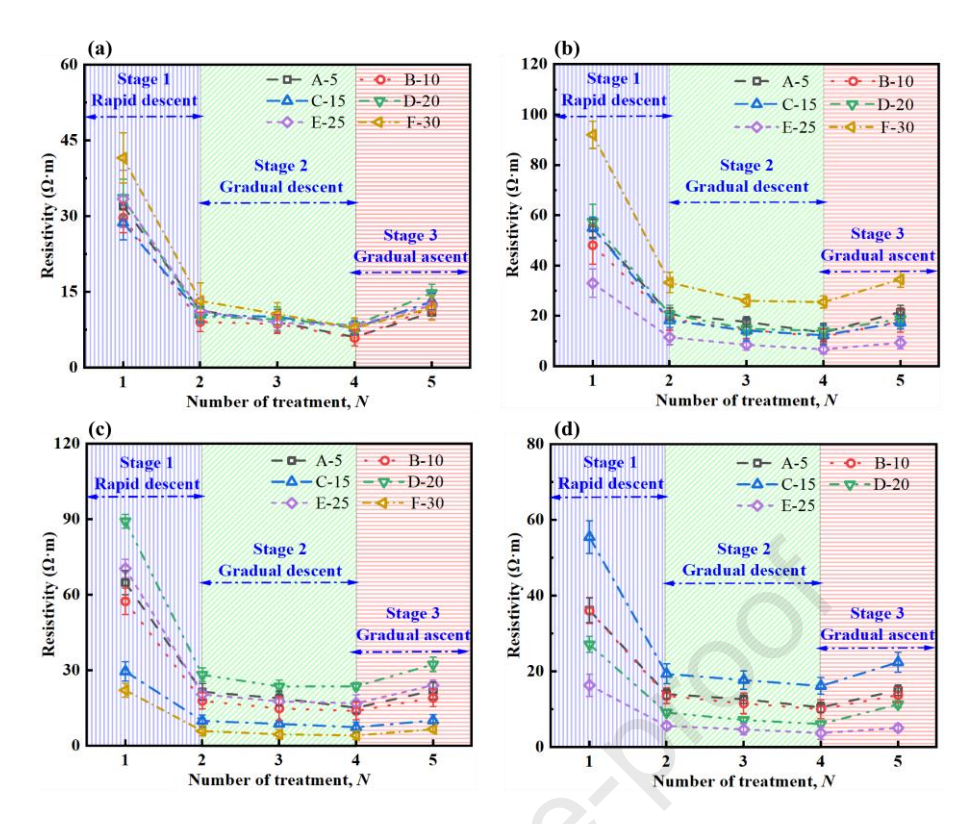


Fig. 11. Variations of sand resistivity under depths and locations: (a) 1st layer; (b) 2nd layer; (c) 3rd layer; and (d) 4th layer.

3.4. Variations of sand resistivity with different cross-sections

Fig. 12 presents the sand resistivity in different cross-sections under the same grouting cycles. The apparent resistivity colors in section I and II are predominantly blue and green, with only small areas exhibiting red and yellow hues. In contrast, section III shows a predominance of red and yellow colors, with limited blue regions. This observation indicates that the mean resistivity values in sections I and II are relatively low, while those in section III are comparatively high. According to the layout of the ERT measurement lines (Fig. 5b), section III is positioned farthest from the grouting pipe, section I is closest, and section II lies between the grouting and suction pipes. The higher average resistivity in section III can be attributed to its greater distance from the grouting pipe, resulting in a lower concentration of EICP solution compared to sections I and II. As previously discussed, sand resistivity in a saturated environment is significantly influenced by ion concentration. The lack of EICP solution in section III leads to a reduced ion concentration, thereby contributing to its higher average resistivity. Conversely, the lower average resistivity values in sections I and II can be explained similarly. Additionally, all three sections exhibit a central region of high resistivity, with section III displaying a larger area of red.

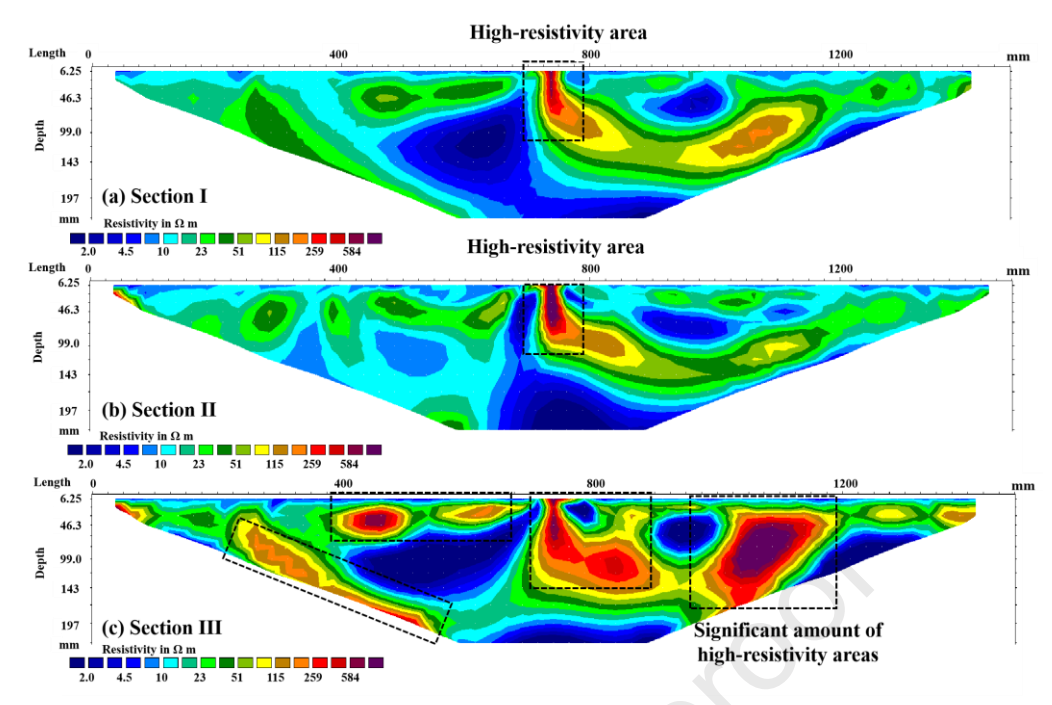


Fig. 12. Variations of sand resistivity at different cross-sections: (a) section I: (b) section II: and (c) section III.

To quantitatively analyze the influence of the aquatic environment on sand resistivity, selected data points from the first and second layers were analyzed, following the pre-established ERT data categorization approach. Fig. 13 presents a comparative diagram of sand resistivity before and after drainage at varying depths and locations. In the first layer, the sand resistivity before drainage remains relatively consistent across different cross-sections, averaging approximately $20~\Omega$ m. In contrast, after drainage, the sand resistivity increases significantly to around $200~\Omega$ m, indicating a nearly tenfold increase. A similar trend is observed in the second layer, where the resistivity difference before and after drainage is also substantial, approaching a tenfold change. This highlights the significant effect of the saturated environment on sand resistivity, as the presence of water and dissolved ions markedly diminishes the resistivity of sand.

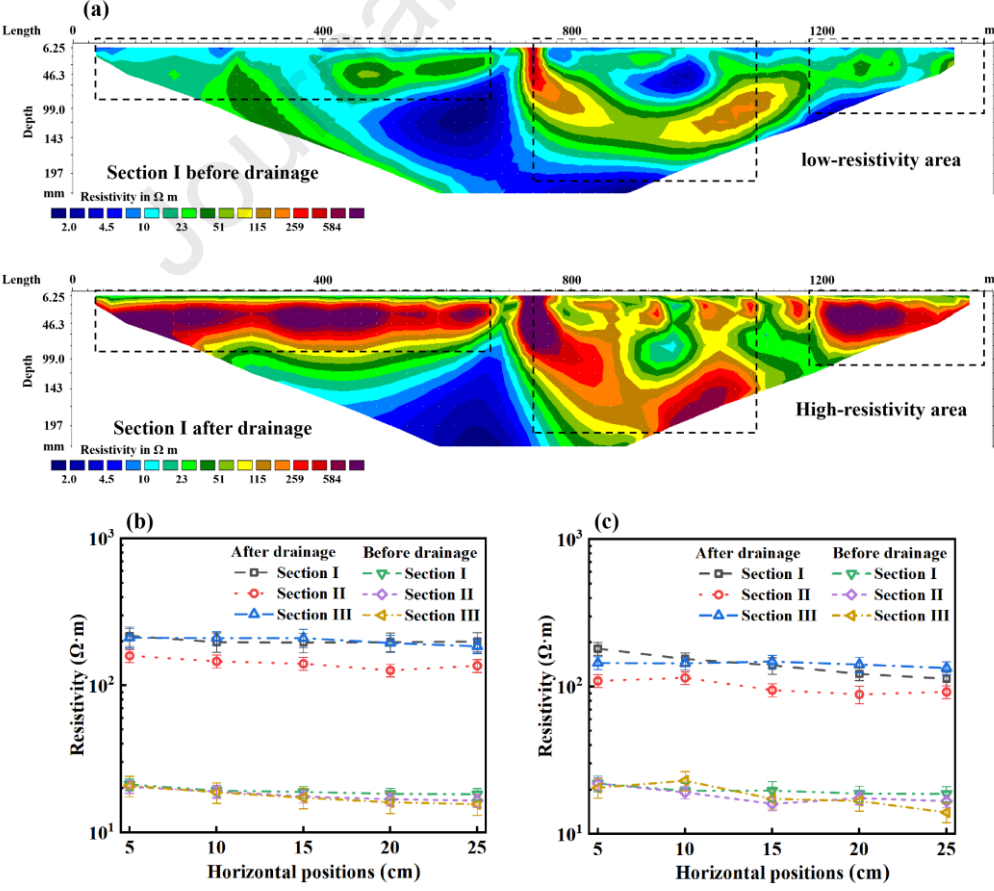


Fig. 13. The resistivity of sand before and after drainage: (a) section I; (b) 1st layer; and (c) 2nd layer.

3.5. Variations of permeability with different grouting cycles

Fig. 14 illustrates the changes in model permeability across different grouting cycles. As the number of reinforcement cycles increases, model permeability experiences a dramatic decline from an initial value of 1.28×10^{-2} m/s to 9.66×10^{-5} m/s, representing a reduction of approximately three orders of magnitude. This significant decrease is primarily attributed to the precipitation of CaCO₃ crystals between sand grains, which reduces porosity and obstructs seepage pathways, thus diminishing permeability. This observation confirms the successful occurrence of urease-catalyzed urea hydrolysis during the model tests, leading to CaCO₃ production.

During the first six grouting cycles, permeability decreases at a consistent rate, largely due to the filling of numerous voids in the sand. In the subsequent cycles (6th-8th), a more pronounced reduction is observed, with permeability dropping from 8.2×10^{-4} m/s to 1.01×10^{-4} m/s, nearly a one-order-of-magnitude decrease. This notable shift can be explained by the fact that most pore spaces have already been filled by the 6th cycle. During the 6th-8th cycles, the deposited $CaCO_3$ begins to cement sand particles together, transitioning from merely filling pores to enhancing the structural integrity of the sand matrix. This cementation restricts many seepage channels, leading to a further substantial decline in model permeability. From 8th to 10th cycles, however, permeability remains relatively stable, experiencing only a slight decrease of 4.4×10^{-6} m/s. This minimal change can be attributed to the earlier $CaCO_3$ crystals blocking most seepage channels, which impedes further penetration of subsequent EICP solutions into the sand. As a result, the already clogged pathways limit any significant changes to permeability.

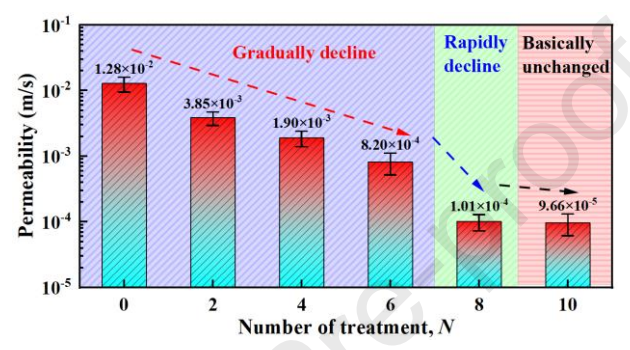


Fig. 14. Permeability of model under different grouting cycles.

3.6. Microscopic analysis

To analyze the microscopic characteristics of EICP-treated sand at varying distances from the grouting pipe, samples were collected from three distinct zones: close to the grouting pipe, between the grouting and suction pipes, and far from the grouting pipe. Fig. 15 presents the SEM images of EICP-treated sand across these different locations. In Fig. 15a, the sample nearest to the grouting pipe reveals numerous $CaCO_3$ crystals on the surfaces of sand grains and at inter-grain contacts. When magnified to $5000 \times$, tightly cemented $CaCO_3$ crystals become apparent, indicating significant crystal formation and effective cementation in this area. This observation corroborates previous findings related to solution conductivity and sand resistivity.

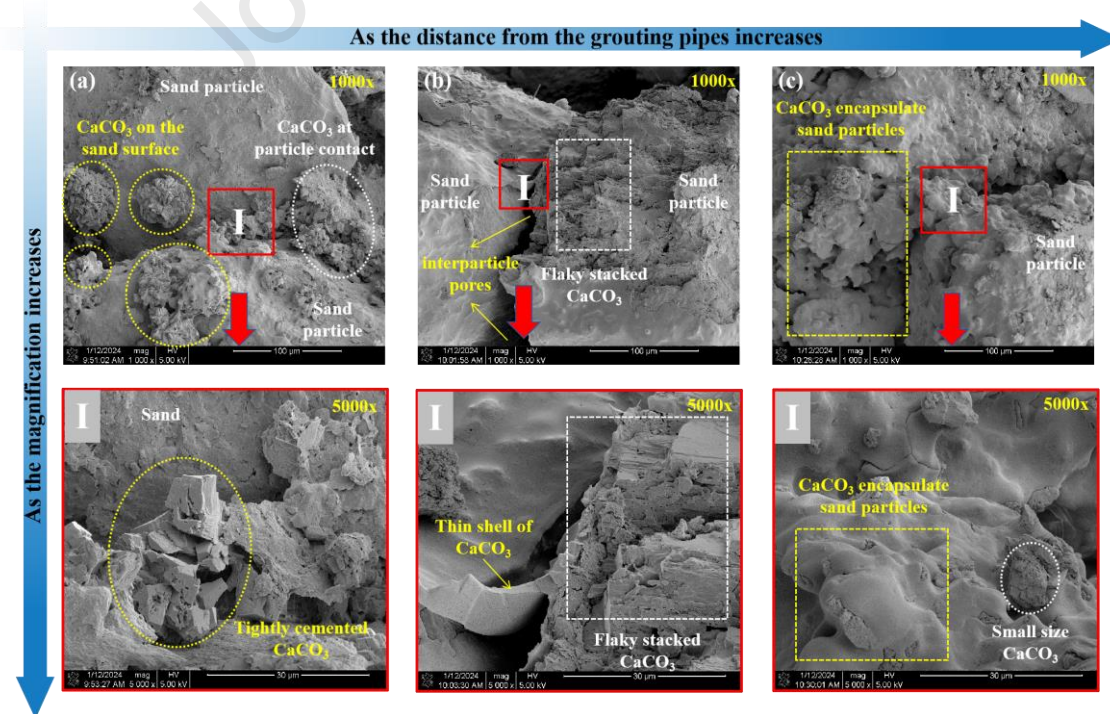


Fig. 15. SEM diagram of EICP treated sand with different distance from the grouting pipe: (a) near grouting pipe; (b) between extraction pipe and grouting pipe; (c) far from grouting pipe

Fig. 15b depicts the intermediate zone. At a magnification of $1000\times$, a few small, spherical $CaCO_3$ crystals and layered, plate-like structures can be seen. At $5000\times$, thin $CaCO_3$ shells (approximately 3 μ m thick) and irregular, plate-like crystals are clearly visible. In contrast, Fig. 15c represents the sample from far from the grouting pipe. At $1000\times$, no significant large $CaCO_3$ crystals are observable. At $5000\times$, the sand grains are only sparsely coated with a thin layer of $CaCO_3$ crystals, and only a few tiny crystals can be observed. This indicates that the $CaCO_3$ production is limited and the cementation effect is weakened in this region, which is consistent with the earlier conductivity and resistivity results. In summary, $CaCO_3$ crystals formation decreases with increasing distance from the grouting pipe. This decrease can be ascribed to lower concentrations of urease and cementitious solutions in areas farther from the grouting pipe, resulting in reduced urease-induced crystallization.

4. Discussion

4.1. Growth pattern of CaCO3 crystals in model tests

The EICP technique is based on urease-catalyzed urea hydrolysis, which generates CO_3^{2-} that subsequently react with Ca^{2+} to form $CaCO_3$ crystals (e.g. Park et al., 2014; Nam et al., 2015). These crystals act as a cementing agent for loose sand particles, and their formation is crucial for enhancing the strength of the sand. Fig. 16 illustrates the growth pattern of $CaCO_3$ crystals, showing that these crystals expand radially outward from the center of the grouting pipe as the number of grouting cycles increases. The cementation area also expands outward from the center of the grouting pipe, which is consistent with the earlier findings derived from the sand resistivity results. However, the resistivity data indicate that although the cementation zones expand around the grouting holes, there are variations in their extents and directions. This discrepancy can be ascribed to spatial variations in sand compactness and porosity at various locations, which affect the diffusion paths of the EICP solution.

Two distinct forms of CaCO₃ precipitation are observed in Fig. 16: deposition on particle surfaces and inter-particle deposition. These forms exhibit different effects based on their deposition locations. The filling effect, characterized by a reduction in pore volume, occurs throughout the EICP mineralization reaction, indicating that all CaCO₃ crystals contribute to this function. In contrast, the cementation effect arises when CaCO₃ crystals deposit between sand particles, bonding adjacent grains together. It is important to note that the filling and cementation effects of CaCO₃ crystals are dynamic. Initially, crystals deposited on sand surfaces primarily serve a filling function. However, as the size of the crystals increases, they come into contact with and bond to adjacent sand particles, transitioning from filling effect to cementation effect. In summary, these two forms of CaCO₃ precipitation play distinct roles in consolidating sand: the filling effect reduces internal pore volume, while the cementation effect enhances the structural integrity and strength of the sand.

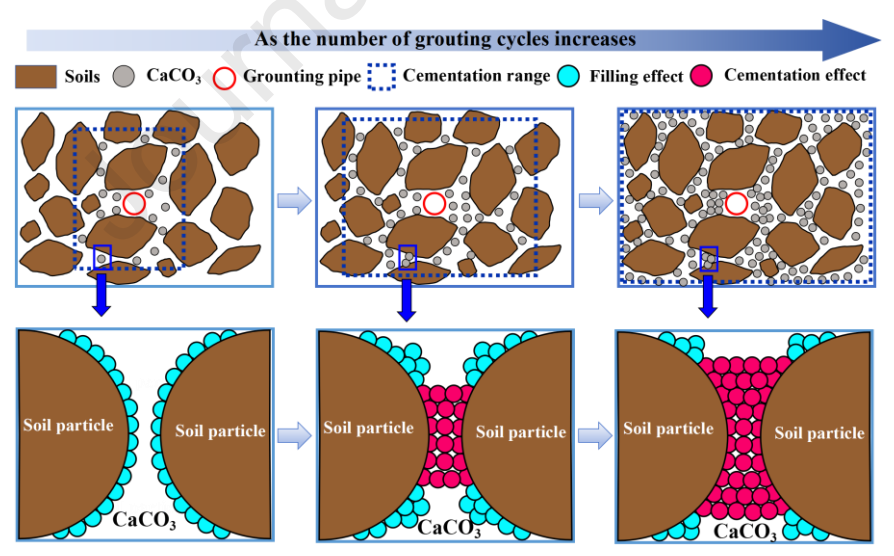


Fig. 16. Schematic of the growth pattern of $CaCO_3$ crystals.

4.2. Effect of CaCO₃ precipitation on sand electrical conductivity

This section discusses the phenomenon and examines the mechanisms by which $CaCO_3$ precipitation affects sand resistivity. During the initial stages of grouting, the resistivity of the sand exhibits the significant decrease, falling from approximately $30~\Omega$ m to around $10~\Omega$ m, indicating a decline of nearly $20~\Omega$ m (see Fig. 11a). However, in the later stages of grouting, an opposite trend is observed, with resistivity values rising with subsequent grouting cycles. For example, at location A, the resistivity after the fourth grouting cycle is $6.08~\Omega$ m, which increases to $10.94~\Omega$ m following the fifth grouting cycle, indicating a rise of $4.86~\Omega$ m. Similar patterns are observed across various depths and horizontal positions, indicating that this phenomenon is consistent and not merely a result of experimental error. This observation aligns with Fig. 17,

which illustrates the impact of CaCO₃ precipitation on sand resistivity. The influence of CaCO₃ in a saturated environment can be examined from two perspectives: the filling effect and the cementation effect of CaCO₃ crystals. First, concerning the filling effect, CaCO₃ fills the voids between sand grains, thereby reducing sand porosity. Since the resistivity of the solution is significantly lower than that of solid materials such as sand and CaCO₃, an electrical current preferentially flows through regions of lower resistivity. The presence of CaCO₃ crystals on the surfaces of sand grains narrows the electric pathways, making current flow more challenging in these areas (Fig. 17a). Second, considering the cementation effect, the precipitation of CaCO₃ between sand particles binds them into a cohesive mass. This cementation effectively obstructs certain current paths, altering the initial optimal conduction routes, and hindering current flow within the affected zones of the sand. Consequently, both the filling and cementation effects of calcium carbonate crystals contribute to an increase in sand resistivity. As CaCO₃ crystals generate, they narrow the current channels and obstruct current pathways. Thus, during the later stages of grouting, the gradual increase in CaCO₃ content results in a progressive rise in sand resistivity.

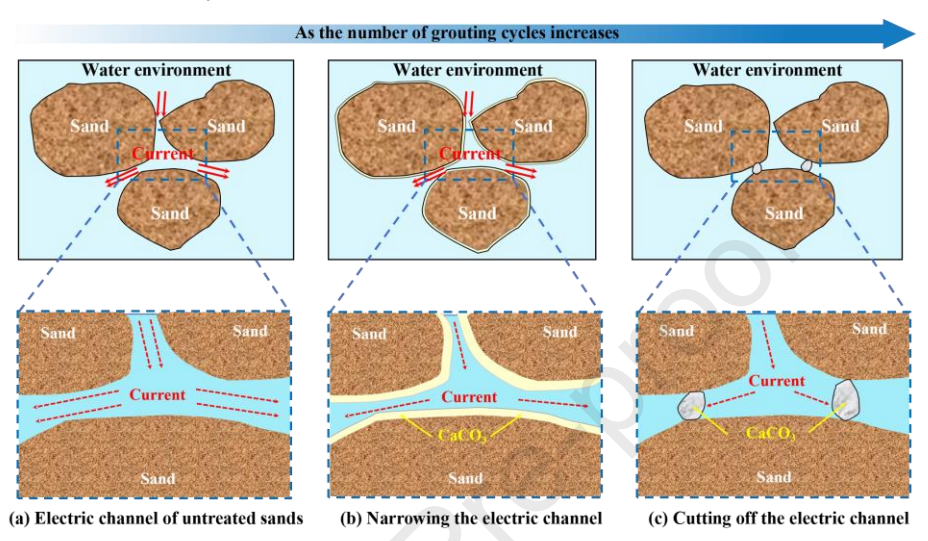


Fig. 17. Influence of CaCO3 precipitation on sand resistivity: (a) Electric channel of untreated sands, (b) Narrowing the electric channel, and (c) Cutting off the electric channel.

4.3. Limitations and implications of current work

The main objective of the present study was to investigate the effectiveness of the EICP technique in reinforcing underwater sand beds. However, the present study still has limitations: Firstly, the model box system employed in this study may not fully represent the complex conditions of real-world underwater environments. Therefore, further research is required to verify these findings in larger-scale or more realistic settings. Secondly, this study focused on a specific set of parameters and did not investigate the influence of other potential factors, such as temperature, pressure, and the presence of other ions. Future research could explore the impact of these additional factors on the performance of the EICP technique. Additionally, ensuring uniform CaCO₃ precipitation in large-scale underwater environments, understanding the long-term durability of treated soils, and assessing the potential environmental impact of enzyme usage in marine ecosystems are crucial areas for future research. Future studies could focus on optimizing the parameters of EICP treatment, such as enzyme concentration, injection techniques, and reaction time, to maximize efficiency in various underwater soil types. Nevertheless, the findings from this study provide a theoretical basis for the application of EICP technology in geotechnical engineering to strengthen seabed foundations and support marine infrastructure. It encourages further investigation to address these limitations and expand the understanding of this technique.

5. Conclusions

In this study, the feasibility of the EICP technique for reinforcing the underwater sand bed was explored through model tests. A model box system and an "injection-extraction" system were designed to facilitate the flow of the EICP solution through the underwater sand layers. The reinforcement effects were evaluated using permeability, ERT, solution conductivity, pH, Ca²⁺ concentration, and SEM tests. The conclusions of the study are summarized as follows:

- (1) The "injection-extraction" system has proven to be an effective method for facilitating the flow of the EICP solution within water-rich sandy layers. The permeability of the model decreases from 1.28×10⁻² m/s to 9.66×10⁻⁵ m/s, a reduction of approximately three orders of magnitude. This verifies that the EICP technology can greatly reduce the permeability of underwater sand beds.
- (2) With increasing grouting cycles, the sand resistivity in a saturated environment initially decreases due to the rising ion concentration in the solution. Subsequently, the sand resistivity increases as CaCO₃ crystals form, which both narrow the
- (3) ERT confirms the intrinsic heterogeneity of the EICP technique in reinforcing large-scale specimens. The resistivity distribution revealed significant spatial variability, with lower values near grouting pipes indicating higher EICP solution concentrations. These variations in resistivity were observed across different depths and locations.
- (4) The precipitation of CaCO₃ crystals between sand particles is not static. As the crystals grow larger, they occupy voids and act as a binding agent that cements the sand particles together. This process is crucial for the long-term stabilization of the sand.

Declaration of competing interest

The authors declare that they have no known competing financial interests or personal relationships that could have appeared to influence the work reported in this paper.

Data availability

The data that support the findings of this study are available from the corresponding author upon reasonable request.

Acknowledgments

This work was supported by the National Youth Top-notch Talent Support Program of China (Grant No. 00389335), the National Natural Science Foundation of China (Grant No. 52378392), and the "Foal Eagle Program" Youth Top-notch Talent Project of Fujian Province (Grant No. 00387088). Their financial supports are gratefully acknowledged.

Credit authorship contribution statement

Qiwu Jiang: Writing-Original Draft, Data Curation, Formal Analysis, Investigation, Methodology, Software, Validation, Visualization, Conceptualization. **Ming Huang**: Resources, Project administration, Funding acquisition, Conceptualization, Supervision, Writing-review & editing. **Jim S. Shiau**: Writing-Review & Editing, Supervision. **Ling Yang**: Writing-original draft, Investigation. **Mingjuan Cui**: Writing-review & editing, Supervision. **Guixiao Jin**: Supervision. **Bincai Huang**: Conceptualization. **Xiaoping Zhang**: Supervision.

References

Arab, M., Rohy, H., Zeiada, W., Almajed, A., Omar, M., 2021. One-phase EICP biotreatment of sand exposed to various environmental conditions. J. Mater. Civ. Eng. 33 (3), 04020489.

Bearce, R. G., Mooney, M. A., Kessouri, P., 2016. Electrical resistivity imaging of laboratory soilcrete column geometry. J. Geotech. Geoenviron. Eng. 142 (3), 04015088.

Cheng, L., Shahin, M. A., Mujah, D., 2017. Influence of key environmental conditions on microbially induced cementation for soil stabilization. J. Geotech. Geoenviron. Eng. 143 (1), 04016083.

Choi, S. G., Park, S. S., Wu, S. F., Chu, J., 2017. Methods for calcium carbonate content measurement of biocemented soils. J. Mater. Civ. Eng. 29 (11), 06017015.

Chu, J., Ivanov, V. M., Stabnikov, V., Li, B., 2013. Microbial method for construction of an aquaculture pond in sand. Geotechnique 63 (10), 871-875.

Cui, M. J., Lai, H. J., Hoang, T., Chu, J., 2021. One-phase-low-pH enzyme induced carbonate precipitation (EICP) method for soil improvement. Acta Geotech. 16 (8), 481-489.

Cui, M. J., Lai, H. J., Wu, S. F., Chu, J., 2024. Comparison of soil improvement methods using crude soybean enzyme, bacterial enzyme or bacteria-induced carbonate precipitation. Geotechique 74 (1), 18-26.

Do, J., Montoya, B. M., Gabr. M. A., 2019. Debonding of microbially-induced carbonate precipitation-Stabilized sand by shearing and erosion. Geomech. Eng. 17 (5), 429-438.

Gao, Y. F., Tang, X. Y., Chu, J., He, J., 2019a. Microbially induced calcite precipitation for seepage control in sandy soil. Geomicrobiol. J. 36 (10), 366-375.

Gao, Y. F., He, J., Tang, X. Y., Chu, J., 2019b. Calcium carbonate precipitation catalyzed by soybean urease as an improvement method for fine-grained soil, Soils Found. 59 (5), 1631-1637.

 $GB/T\ 14684-2011,\ 2011.\ Sand\ for\ Construction.\ Standards\ Press\ of\ China,\ Beijing,\ China\ (in\ Chinese).$

Gomez, M. G., Anderson, C. M., Graddy, C. M., et al., 2017. Large-scale comparison of bioaugmentation and biostimulation approaches for biocementation of sands. J. Geotech. Geoenviron. Eng. 143 (5), 04016124.

Hafidz, A., Kinoshita, N., Yasuhara H., 2024. Effect of permeants on fracture permeability in granite under hydrothermal conditions. Rock Mech. Bull. 1 (1), 100007.

Huang, M., Xu, K., Xu, C. S., Jin, G. X., Guo, S., 2021. Micromechanical properties of biocemented shale soils analyzed using nanoindentation test. J. Geotech. Geoenviron. Eng. 147 (12), 04021157.

Huang, X. S., Zhang, R. J., Zheng, J. J., 2024a. Comparison of the efficiency of traditional MICP and two-step MICP method for immobilizing heavy metals in aquatic environments. Biogeotechnics. (Available online 25 May 2024)

Huang, M., Jiang, Q. W., Xu, K., Xu, C. S., 2024b. Feasibility analysis of EICP technique for reinforcing backfill layer behind TBM tunnel linings based on model tests. Tunn. Undergr. Space Technol. 155 (1), 106172.

JGJ 52—2006, 2006. Standard for Technical Requirements and Test Method of Sand and Crushed Stone (Or Gravel) for Ordinary Concrete. China Architecture and Building Press, Beijing, China (in Chinese).

Jiang, N. J., Yoshioka, H., Yamamoto, K., Soga, K., 2016. Ureolytic activities of a urease-producing bacterium and purified urease enzyme in the anoxic condition: implication for subseafloor sand production control by microbially induced carbonate precipitation (MICP). Ecol. Engng. 90 (4), 96-104.

Jiang, Q. W., Huang, M., Xu, K., Cui, M. J., Li, S., Jin, G. X., 2024a. Statistical damage constitutive model of MICP-treated specimens based on lognormal distribution. Acta Geotech. (Available online 04 January 2025)

Jiang, Q. W., Huang M., Cui M. J., Jin, G. X., Peng, Y. X., 2024b. Study on the mechanism and optimal proportioning test of pea gravel backfill behind TBM tunnel linings reinforced with enzyme-induced calcium carbonate precipitation (EICP) technology. Rock Soil Mech. 45 (7), 2037-2049. (in Chinese)

Khodadadi, T. H., Javadi, N., Krishnan, V., Hamdan, N., Kavazanjian, E., 2020. Crude urease extract for biocementation. J. Mater. Civil. Eng. 32 (12), 04020374.

Lai, H. J., Cui, M. J., Wu, S. F., Yang, Y., Chu, J., 2021. Retarding effect of concentration of cementation on biocementation of soil. Acta Geotech. 16 (5), 1457-1472.

Lai, H. J., Liu, H. Cui, M. J., Zheng, J. J., Chen, Z. B., Zhang, Z. C., 2024. Inorganic flocculant-based soybean urease extraction and its effect on biomineralization. J. Clean. Prod. 460 (11), 142539.

- Li, W. L., Zhang, Y. H., Achal, V., 2022. Mechanisms of cadmium retention on enzyme-induced carbonate precipitation (EICP) of Ca/Mg: Nucleation, chemisorption, and co-precipitation. J. Environ. Chem. Eng. 10 (3), 107507.
- Li, S., Huang M., Cui M. J., Xu, K., Jin, G. X., 2023a. Thermal and mechanical properties of bio-cemented quartz sand mixed with steel slag, Biogeotechnics 1 (3), 100036.
- Li, S., Huang, M., Cui, M. J., Jiang, Q. W., Xu, K., 2023b. Thermal conductivity enhancement of backfill material and soil using enzyme-induced carbonate precipitation (EICP). Acta Geotech. 18 (11), 6143-6158.
- Liu, K. W., Jiang, N. J., Qin, J. D., Wang, Y. J., Tang, C. S., Han, X. L., 2021. An experimental study of mitigating coastal sand dune erosion by microbial-and enzymatic-induced carbonate precipitation. Acta Geotech. 16 (2), 467-480.
- Liu, H. L., Chu, J., Kavazanjian, E., 2023. Biogeotechnics: A new frontier in geotechnical engineering for sustainability, Biogeotechnics 1(1), 100001.
- Liu, H. L., Zhang, J. X., Xiao, Y., He, X., 2024. Bacterial attachment by crystal in MICP. Biogeotechnics 2(4), 100109.
- Loke, M. H., Chambers, J. E., Rucker, D. F., Kuras, O., Wilkinson, P. B., 2013. Recent developments in the direct-current geoelectrical imaging method. J. Appl. Geophys. 95 (8), 135-156.
- Martinez, B. C., DeJong, J. T., Ginn. T. R., 2014. Bio-geochemical reactive transport modeling of microbial induced calcite precipitation to predict the treatment of sand in one-dimensional flow. Comput. Geotech. 58 (11), 1-13.
- Meng, H., Shu, S., Gao, Y. F., Yan, B. Y., He, J., 2021. Multiple-phase enzyme-induced carbonate precipitation (EICP) method for soil improvement. Eng. Geol. 294 (5), 106374.
- Montoya, B. M., Do, J. N., Gabr, M. A., 2021. Distribution and properties of microbially induced carbonate precipitation in underwater sand bed. J. Geotech. Geoenviron. Eng. 147 (10), 04021098.
- Nafisi, A., Safavizadeh, S., Montoya, B. M. 2019. Influence of microbe and enzyme-induced treatments on cemented sand shear response. J. Geotech. Geoenviron. Engng, 145 (9), 06019008
- Nam, I. H., Chon, C. M., Jung, K. Y., Choi, S. G., Choi, H., Park, S. S., 2015. Calcite precipitation by ureolytic plant (Canavalia ensiformis) extracts as effective biomaterials. KSCE J. Civ. Eng 19 (6), 1620-1625.
- Park, S. S., Choi, S. G., Nam, I. H., 2014. Effect of plant-induced calcite precipitation on the strength of sand. J. Mater. Civ. Eng. 26 (8), 06014017.
- Shi, J. Q., Wang, L., Zhang, X. M., et al., 2024. Experimental study on electricity resistivity of MICP-treated calcareous sand foundation. Chin. J. Geotech. 46 (2), 244-253. (in Chinese)
- Song, J. Y., Sim, Y., Jang, J., Hong, W. T., Yun, T. S., 2020. Near-surface soil stabilization by enzyme-induced carbonate precipitation for fugitive dust suppression. Acta Geotech, 15 (7), 1967-1980.
- Sun, X. H., Miao, L. C., Wang, H. X., Yin, W. H., Wu, L. Y., 2021. Mineralization crust field experiment for desert sand solidification based on enzymatic calcification, J. Environ. Manage. 287 (11), 112315.
- Sun, X. H., Wai, O. H., Xie, J. W., Li, X. D., 2023. Biomineralization to prevent microbially induced corrosion on concrete for sustainable marine infrastructure. Environ. Sci. Technol. 58 (1), 522-533.
- Sun, X. H., He, J. L., Cui, H., Shi, J. Q., 2024a. Endeavours to achieve sustainable marine infrastructures: A new "window" for the application of biomineralization in marine engineering. Biogeotechnics 2 (4), 100098.
- Sun, X. H., Miao, L. C., Wang, H. X., Guo, X., Wu, L. Y., 2024b. Control of urease activity in enzyme-induced carbonate precipitation method for soil improvement at high temperatures. Acta Geotech. 19 (11), 7495-7515
- Tucker, S. E., Briaud, J. L., Hurlebaus, S., Everett, M. K., Arjwech, R., 2015. Electrical resistivity and induced polarization imaging for un-known bridge foundations. J. Geotech. Geoenviron. Eng. 141 (5), 04015008.
- Wang, B. H., Wang, Z. H., Jiang, P. M., Zhou, A. Z., 2017. Electrical resistivity characteristics of saturated sand with varied porosities. Chin. J. Geotech. 39 (9), 1739-1745 (in Chinese).
- Wang, K. D., Wu, S. F., Chu, J., 2023a. Mitigation of soil liquefaction using microbial technology: An overview, Biogeotechnics 1 (1), 100005.
- Wang, H. X., Sun, X. H., Miao, L. C., Cao, Z. M., Guo, X., 2023b. Garlic extract addition for soil improvement at various temperatures using enzyme-induced carbonate precipitation (EICP) method. J. Rock Mech. Geotech. Eng. 15 (12), 3230-3243.
- Wang, H. Y., Sharma, M. M., 2024a. Uniquely determine fracture dimension and formation permeability from diagnostic fracture injection test. Rock Mech. Bull. 2 (2), 100040.
- Wang, Y., Sun, X. H., Miao, L. C., et al., 2024b. State-of-the-art review of soil erosion control by MICP and EICP techniques: Problems, applications, and prospects. Sci. Total Environ. 912 (20), 169016.
- Weng, Y. J., Zheng, J. J., Lai, H. J., Cui, M. J., Ding, X. Z., 2024. Biomineralization of soil with crude soybean urease using different calcium salts. J. Rock Mech. Geotech. Eng. 16 (22), 1788–1798.
- Wu, L. Y., Miao, L. C., Sun, X. H., Wang, H. X., 2024. Effect of calcium sources on enzyme-induced carbonate precipitation to solidify desert aeolian sand. J. Environ. Chem. Eng. 366 (1), 121687.
- Xiao, P., Liu, H. L., Xiao, Y., Stuedlein, A., Evans, T. M., 2018. Liquefaction resistance of bio-cemented calcareous sand. Soil Dyn. Earthq. Eng. 107 (18), 9-19.
- Xiao, Y., Chen, H., Stuedlein, A., et al., 2020. Restraint of particle breakage by biotreatment method. J. Geotech. Geoenviron. Eng. 146 (11), 04020123.
- Xu, K., Huang, M., Liu, Z. J., Cui, M. J., Li, S, 2023a. Mechanical properties and disintegration behavior of EICP-reinforced sea sand subjected to drying-wetting cycles. Biogeotechnics 1 (2), 100019.
- Xu, K., Huang, M., Zhen, J. J., Xu, C. S., Cui, M. J., 2023b. Field implementation of EICP Technology for reinforcing a bedding layer beneath an underground cable duct. J. Rock Mech. Geotech. 15 (4), 1011-1022.
- Xu, K, Huang, M, Cui, M. J., Li, S, 2023c. Retarding effect of cementation solution concentration on cementation ability of calcium carbonate crystal induced using crude soybean enzyme. Acta Geotech. 18 (11), 6235-6251.
- Xue, Z. F., Cheng, W. C., Wang, L., Hu, W. L., 2022. Effects of bacterial inoculation and calcium source on microbial-induced carbonate precipitation for lead remediation. J. Hazard. Mater. 15 (426), 128090.
- Yang, T., Guo, B., Lian, J. J., Su, H., Qu, C. L., 2016. Effect of temperature and humidity on the adhesion strength and damage mechanism of shotcrete-surrounded rock. Constr. Build. Mater. 124 (15), 1109-1119.

- Zamani, A., Montoya, B. M., Gabr, M. A., 2019. Investigating challenges of in situ delivery of microbial-induced calcium carbonate precipitation (MICP) in fine-grain sands and silty sand. Can. Geotech. J. 56 (12), 1889-1900.
- Zeng, C., Veenis, Y., Hall, C. A., et al., 2021. Experimental and numerical analysis of a field trial application of microbially induced calcite precipitation for ground stabilization. J. Geotech. Geoenviron. Eng. 147 (7), 05021003.
- Zeng, C., Van Paassen. L., Zheng, J. J., et al., 2022. Soil stabilization with microbially induced desaturation and precipitation (MIDP) by denitrification: a field study. Acta Geotech. 17 (12), 5359-5374.
- Zhang, S. H., Li, Y., Kou, X. H., Dong, X. Q., 2015. Study of electrical resistivity and strength characteristics of zinc contaminated soil solidified by cement. Rock Soil Mech. 36 (10), 2899-2906. (in Chinese)
- Zhang, J. Z., Tang, C. S., Zhu C., Zhou, Q. Y., Xu, J. J., Shi, B., 2023b. Monitoring and mapping the evolution of clayey soil desiccation cracking using electrical resistivity tomography. Bull. Eng. Geol. Environ. 82 (11), 1-16.
- Zhang, Y., Hu, X. L., Wang, Y. J., Jiang, N. J., 2023a. A critical review of biomineralization in environmental geotechnics: Applications, trends, and perspectives, Biogeotechnics 1 (1), 100003.
- Zhang, J. Z., Tang, C. S., Lu, C., Zhou, Q. Y., Shi, B., 2024. Monitoring and characterizing the whole process of microbially induced calcium carbonate precipitation using electrical resistivity tomography. J. Geotech. Geoenviron. Eng. 150 (1), 04023132.



Dr. Qiwu Jiang received the MSc degree from the College of Civil Engineering, Fuzhou University. His supervisor is Prof. Ming Huang. He is pursuing his PhD in College of Civil Engineering, Wuhan University, China. His research focuses on seepage characteristics of bio-cemented soils and EICP/MICP-based environment-friendly ground reinforcement methods. He has published more than ten scientific papers.

Declaration of interests

| ☑ The authors declare that they have no known competing financial interests or personal relationships hat could have appeared to influence the work reported in this paper. |
|---|
| □The authors declare the following financial interests/personal relationships which may be considered as potential competing interests: |
| |